ACSNANO
www.acsnano.org
ARTICLE

Graphene Oxide Nanosheets Reshape Synaptic Function in Cultured Brain Networks

Rossana Rauti,[†] Neus Lozano,[‡] Veronica León,[§] Denis Scaini,[†,⊥] Mattia Musto,[∥] Ilaria Rago,[⊥] Francesco P. Ulloa Severino,[∥] Alessandra Fabbro,[¶] Loredana Casalis,[⊥] Ester Vázquez,[§] Kostas Kostarelos,[‡] Maurizio Prato,[*,¶,#,△] and Laura Ballerini[*,†,∥]

[†]Life Science Department, University of Trieste, 34127 Trieste, Italy

[‡]Nanomedicine Lab, School of Medicine and National Graphene Institute, Faculty of Medical & Human Sciences, University of Manchester, M13 9PL Manchester, United Kingdom

[§]Departamento de Química Orgánica, Facultad de Ciencias y Tecnologías Químicas-IRICA, Universidad de Castilla La Mancha, 13071 Ciudad Real, Spain

[⊥]ELETTRA Synchrotron Light Source, 34149 Trieste, Italy

[∥]International School for Advanced Studies (SISSA), 34136 Trieste, Italy

[¶]Department of Chemical and Pharmaceutical Sciences, University of Trieste, 34127 Trieste, Italy

[#]CIC BiomaGUNE, Parque Tecnológico de San Sebastián, Paseo Miramón, 182, 20009 San Sebastián, Guipúzcoa, Spain

[△]Basque Foundation for Science, Ikerbasque, Bilbao 48013, Spain

Supporting Information

ABSTRACT: **Graphene offers promising advantages for biomedical applications. However, adoption of graphene technology in biomedicine also poses important challenges in terms of understanding cell responses, cellular uptake, or the intracellular fate of soluble graphene derivatives. In the biological microenvironment, graphene nanosheets might interact with exposed cellular and subcellular structures, resulting in unexpected regulation of sophisticated biological signaling. More broadly, biomedical devices based on the design of these 2D planar nanostructures for interventions in the central nervous system require an accurate understanding of their interactions with the neuronal milieu. Here, we describe the ability of graphene oxide nanosheets to down-regulate neuronal signaling without affecting cell viability.**

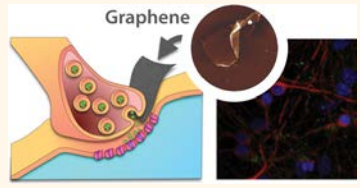

KEYWORDS: *nanotechnology, graphene, patch-clamp, synaptic terminals, exocytosis, FMI-43, microvesicles*

Graphene is a 2D plate-like material consisting of sp^2-hybridized carbon atoms organized in a hexagonal lattice and characterized by, among other properties, high electron mobility and mechanical flexibility.[1−3] In addition to the successful exploitation of graphene and graphene-based materials in an increasing number of industrial products, current applications of graphene hold the potential to revolutionize specific areas of medicine.[2−6] Biomedical developments, in general, in neurology, in particular, are focusing on few-layer graphene sheets to manufacture novel biodevices, including biosensors, interfaces, tissue scaffolds, drug delivery, and gene therapy vector systems.[4] The successful design of multifunctional graphene-based neurodevices will expose brain cells and neuronal circuits directly to this material by injection or implantation.[4,7] In this context, the exploration of the interactions between graphene nano- and microsheets with the sophisticated signaling machinery of nerve cells, with a particular focus on potential graphene flake interactions with the hydrophobic membrane domains, is of great importance.[1,8,9] Such interactions may favor graphene translocation or adhesion to cell membranes,[8,10] potentially interfering with exquisite membrane activities, such as the exocytic and endocytic trafficking systems, which are crucial to physiological synaptic transmission.[8,11]

Here, we explore by patch clamp and fluorescence imaging the ability of graphene (GR) and graphene oxide (GO) nanosheets to interfere with synaptic signaling once hippocampal cultured neurons are exposed for 1 week to a growth medium containing thin sheets of such materials at 1 or 10 μg/mL (concentrations reported not to induce cell death[12−14]). We further investigated whether, in the absence of explicit cell toxicity, such materials affected the ability of astrocytes to release synaptic-like microvesicles[15] (MVs) in pure glial cultures. Our results describe the potential of GO nanosheets to alter different modes of interneuronal communication systems in the central nervous system (CNS), hinting at

Received: January 7, 2016
Accepted: March 31, 2016
Published: March 31, 2016

© 2016 American Chemical Society

DOI: 10.1021/acsnano.6b00130
ACS Nano 2016, 10, 4459−4471

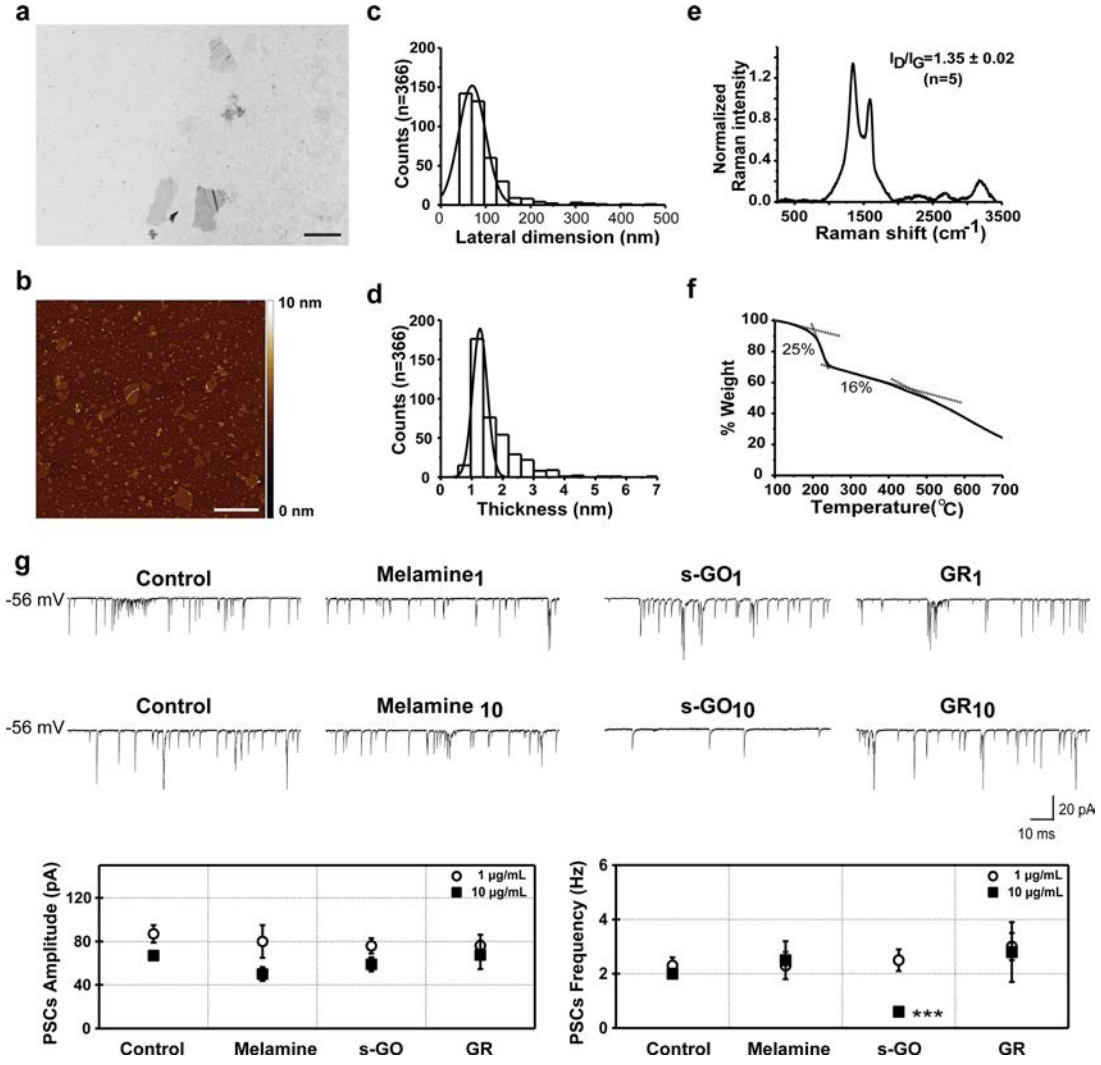

Figure 1. Characterization of small graphene oxide (s-GO) of biological grade; graphene oxide exposure at high concentration influences synaptic function. (a–f) Physicochemical characterization of s-GO: (a) TEM micrograph (scale bar 1 μm), (b) AFM height image (scale bar 1 μm), (c) lateral dimension distribution, and (d) thickness distribution analysis; (e) normalized Raman spectrum and (f) TGA analysis. (g) Graphene oxide exposure at high concentration influences synaptic function. Spontaneous synaptic activity recorded from hippocampal cultures in control, melamine, s-GO, and GR-treated cultures at 1 μg/mL (top traces) and 10 μg/mL (bottom traces) grown for 8–10 days *in vitro*. Postsynaptic currents (PSCs) were detected at −56 mV holding potential. Bottom plots represent pooled data and summarize average PSC amplitude and frequency; note the reduction in s-GO treatment (10 μg/mL, final concentration) of PSC frequency (* = $P < 0.001$ Student's *t* test; data are mean ± SEM).**

opportunities for neuromodulatory applications or highlighting subtle, but potentially unwanted, subcellular interactions.

RESULTS AND DISCUSSION

To address the issue of prolonged exposure of a functional brain network to graphene sheets, we used different materials. Graphene oxide sheets of large and small lateral dimensions (l-GO and s-GO, respectively) were synthesized using a modified Hummers method (see Methods). Following the reaction, the GO gel-like top layer was extracted carefully by using warm water, resulting in the large GO (l-GO). Final concentrations ranging between 1 and 2 mg/mL were obtained with a yield of *ca.* 10%. l-GO was freeze-dried, reconstituted in water for injection, sonicated for 5 min, and centrifuged at room temperature to generate the small GO (s-GO).The lateral dimension of the GO sheets was controlled by drying and sonicating the l-GO to obtain the s-GO sheets, which were always at least 1 order of magnitude smaller, without introducing any significant changes among their surface properties (see Table S1 in the Supporting Information).

The GO dispersions in aqueous media were homogeneous, of brownish color, and stable at room temperature for more than 6 months. The physicochemical characterization of the l-GO and s-GO dispersions is shown in Figure 1a–f and in the Supporting Information Figures S1 and S2. The structural properties (lateral dimension and thickness) were studied by optical microscopy, transmission electron microscopy (TEM), and atomic force microscopy (AFM). Optical properties were studied by UV–vis and fluorescence spectroscopy. Raman spectroscopy and laser Doppler electrophoresis (measuring ζ-potential) were used to assess the surface properties of the GO materials. The Raman spectroscopic analysis revealed D and G bands at 1319 and 1596 cm^{-1}, respectively, characteristic of most polyaromatic hydrocarbons. The D to G band intensity ratio (I_D/I_G) was calculated to be 1.3, corresponding to the metric of disorder in the graphitic structure. The surface charge

DOI: 10.1021/acsnano.6b00130
ACS Nano 2016, 10, 4459–4471

measured with a Zetasizer instrument showed an average ζ-potential of −50 mV, indicating flakes of high negative surface charge. To elucidate the degree of surface functionalization, thermogravimetric analysis (TGA) and X-ray photoelectron spectroscopy (XPS) were performed to quantify the purity of the GO (>99%) and the C/O ratio. XPS high-resolution C 1s spectra were recorded to elucidate the contribution of individual functional groups such as carboxylic, carbonyl, epoxide, and hydroxyl (Table S2b). All fittings shown were performed using the CasaXPS software, and the different regions were assigned according to NIST's XPS and lasurface databases. Deconvolution XPS spectra and assignment of the functional groups indicated that hydroxyls were the least abundant species in the GO material (see Supporting Information Table S2a).

Aqueous dispersions of graphene flakes were prepared using ball-milling for the exfoliation of graphite through interaction with melamine, as previously described[16,17] (see Methods). Due to the GR preparation process, graphene dispersions can contain traces of melamine. In order to determine the exact amount of these traces, final graphene dispersions (0.09 mg/mL) were evaluated by elemental analysis, which indicated 0.9 ppm of melamine. Experiments that involved incubation in neurons also included controls exposed to equal amounts of melamine alone (see Methods). The physicochemical characterization of GR dispersions is shown in Figure S3. The lateral size, studied by TEM, was found to range between 500 nm and 3 μm (Figure S3a,b in the Supporting Information). Optical properties were studied by UV−vis absorption spectroscopy. Dispersions were diluted, and the respective UV−vis absorption spectra were recorded (Figure S3). The spectra are featureless in the vis−NIR region, as expected. The absorbance at 660 nm, divided by cell length, is plotted against the concentration, exhibiting Lambert−Beer behavior (Figure S3d). Raman spectroscopy revealed differences between the GO and GR. Graphene exhibits G and 2D modes around 1573 and 2700 cm^{-1} that satisfy Raman selection rules, while the D peak, around 1345 cm^{-1}, requires a defect for its activation (Figure S3e). The D to G band intensity ratio was calculated at different locations, giving a significantly low value (0.22) in comparison with that of GO. TGA was also used to quantify the functionalization degree of GR. The low weight loss observed in GR (7%) corroborated the low quantity of oxygen groups generated by the exfoliation process (Figure S3f).

We used hippocampal neurons isolated and cultured for 8−10 days *in vitro* (DIV). Primary neuronal cultures were incubated for 2 DIV in the presence of GR or s-GO (at 1 and 10 μg/mL; see Methods) and maintained for 6−8 days. Afterward, visually identified neurons were patch clamped under a voltage clamp. Hippocampal neuron maturation and viability were assessed using single-cell recordings (see Methods) to measure the cell passive membrane properties that are accepted indicators of neuronal health[18−20] that allowed comparison among the recorded cells. These parameters (membrane capacitance and input resistance) displayed similar values in all treatment conditions (summarized in Table 1).

To investigate synapse formation and activity after *in vitro* growth of neurons, we monitored the occurrence of spontaneous postsynaptic currents (PSCs). The appearance of PSCs provided clear evidence of functional synapse formation, and it is a widely accepted index of network efficacy.[21,22]

Table 1. Neuronal Passive Membrane Properties upon GR and s-GO Exposure (1 and 10 μg/mL, Respectively)

	capacitance (pF)	input resistance (MΩ)
$control_1$ (n = 24)	59 ± 4	976 ± 138
$melamine_1$ (n = 28)	46 ± 5	1036 ± 132
$s\text{-}GO_1$ (n = 27)	62 ± 8	876 ± 145
GR_1 (n = 30)	50 ± 5	1029 ± 161
$control_{10}$ (n = 20)	57 ± 7	744 ± 82
$melamine_{10}$ (n = 25)	72 ± 16	717 ± 106
$s\text{-}GO_{10}$ (n = 18)	67 ± 6	997 ± 156
GR_{10} (n = 25)	59 ± 18	1223 ± 501

Figure 1g shows representative current tracings of the recorded electrical activity. In neurons exposed to low (1 μg/mL) s-GO and GR, spontaneous synaptic activity was not affected. In fact, measured PSC amplitude and frequency in s-GO and GR (79 ± 7 pA, 2.5 ± 0.4 Hz, n = 27 and 77 ± 8 pA, 3 ± 0.5 Hz, n = 30, respectively) were comparable to the corresponding control and control−melamine values (87 ± 8 pA and 2.3 ± 0.3 Hz, control, n = 24; 80 ± 15 pA and 2.3 ± 0.5 Hz melamine n = 28; plots in Figure 1g). In all tests, cell parameters measured in melamine were comparable to those expressed by control neurons (Figure 1g, bottom plots), thus the impact on cells of such a contaminant at the estimated concentration is negligible.

When investigating the impact of higher graphene doses (10 μg/mL), we detected a significant difference (P < 0.001; Student's t test) in PSC frequency when comparing control neurons (2.0 ± 0.1 Hz control, n = 20) with s-GO-treated ones (0.6 ± 0.1 Hz, n = 18), while in melamine and GR, PSC frequency values remained unchanged (2.5 ± 0.7 Hz, n = 25 for melamine and 2.8 ± 1.1 Hz, n = 25 for GR). In all treatments studied, the amplitude values of the PSCs were never affected (data are summarized in Figure 1g plots). We further tested synaptic responses when neurons were treated (1 and 10 μg/mL) with a commercially available GO provided by an industrial partner (A-GO; Supporting Information and Figure S4). Similar reduction in PSC frequency (Figure S5) was detected that validated the observation that GO nanosheets, differently than GR flakes, specifically interfered with synapses in cultured neurons, regardless of the starting material.

The impact of 10 μg/mL s-GO on synaptic activity was not related to a decreased number of surviving neurons in the presence of s-GO. In fact, we determined the cellular composition of control and s-GO-treated hippocampal cultures using immunofluorescence markers[23] for astrocytes (GFAP) and neurons (β-tubulin III). We observed both β-tubulin III and GFAP immunoreactive cells in all growing conditions (Figure 2a), and both cell groups were represented in a comparable proportion in all treatment groups (quantified by measuring the cell density in Figure 2a; n = 13 visual field per condition, three different culture series). Thus, s-GO at higher concentrations specifically altered synapse formation and/or function without affecting cell survival or the global network size.

To gain more insight into such processes, we further investigated s-GO-treated (10 μg/mL) cultures. We specifically addressed the distribution of neuronal excitation by measuring the activity of small clusters of neurons with fluorescence calcium imaging.[23−25] On average, 7 ± 2 fluorescent neurons (n = 26 fields), stained with the membrane-permeable Ca^{2+} dye Fura-2-AM (see Methods), were simultaneously visualized in

DOI: 10.1021/acsnano.6b00130
ACS Nano 2016, 10, 4459−4471

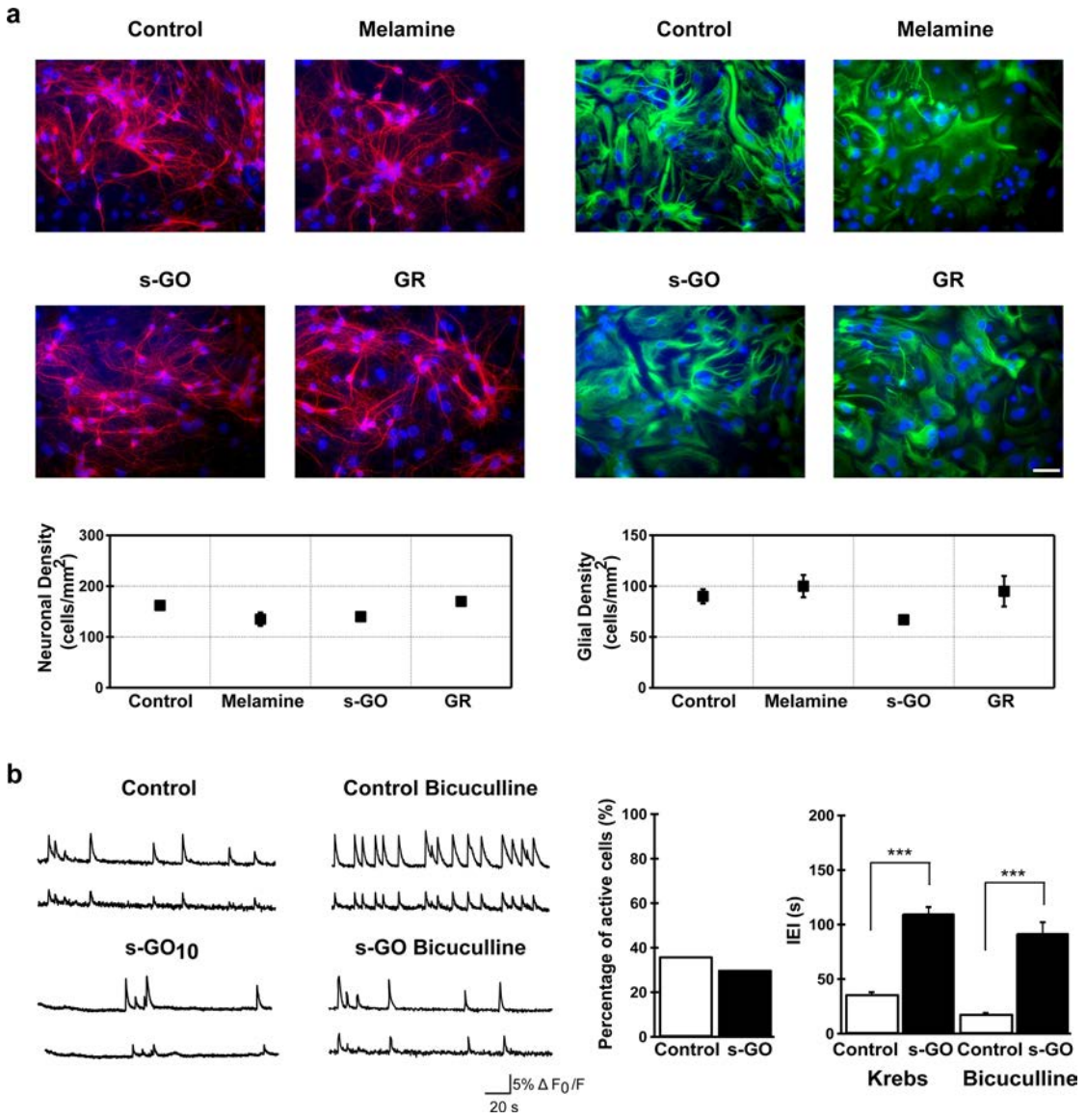

Figure 2. s-GO exposure at high concentration impaired network activity without changing network size. (a) Immunofluorescence images are shown to visualize neurons and glial cells in four different conditions (anti-β-tubulin III, in red, left panels; anti-GFAP, in green, right panels; in all, nuclei are visualized by DAPI in blue) (samples are for the 10 μg/mL protocol; scale bar 50 μm). The plots summarize neuronal (left) and glial (right) densities in all conditions. (b) Repetitive spontaneous Ca^{2+} (left panel) or bicuculline-induced (right panel) oscillations recorded in hippocampal cultures at 8−10 DIV (from each field sample, recordings of two cells were selected). Histograms summarize the percentage of spontaneous active cells (middle) and the average values of the interevent interval (IEI; right) in standard saline (Krebs) and in the presence of bicuculline (* = $P < 0.001$ Student's t test; data are mean ± SEM).**

the recorded field (120 × 160 μm^2). We compared and characterized the cell ability to generate repetitive Ca^{2+} oscillations.[23−25] In control conditions, all recorded fields (n = 8) displayed active cells, while in s-GO-treated cells, 56% (n = 10 out of 18) of the recorded fields did not display detectable cell activity. However, in the remaining s-GO fields (n = 8), we found an amount of neurons that were spontaneously generating repetitive Ca^{2+} oscillations comparable to that measured in controls (Figure 2b; 36% in control, 20 out of 56 neurons, n = 8 active fields and 30% in s-GO-treated, 18 out of 60 neurons, n = 8 active fields).

Figure 2b traces represent fluorescence recordings from active fields in control and s-GO-treated cultures (two sampled cells in each field). Episodes usually comprised spontaneous bursts of activity, fully blocked by tetrodotoxin (TTX, a blocker of voltage-gated, fast Na^+ channels) applications (1 μM; n = 8 fields, control and s-GO-treated; not shown). Control Ca^{2+} oscillations displayed an interevent interval (IEI) of 36 ± 2 s (n = 20 cells) that was significantly lower ($P < 0.001$; Student's t test) than that measured in s-GO-treated networks (110 ± 6 s, n = 18 cells, right plot in Figure 2b). When $GABA_A$ receptors were pharmacologically blocked by bicuculline (20 μM, 20 min), an antagonist of inhibitory connections known to potentiate rhythmic activity patterns,[23,26,27] the control IEI average value was still significantly lower ($P < 0.001$; Student's t test) than that measured in s-GO neurons in the presence of the $GABA_A$ receptor antagonist (18 ± 1 s, n = 20 in control cells *vs* 92 ± 10 s, n = 18 in s-GO cells; plot in Figure 2b, right). This indicated a direct reduction in the excitatory activity due to s-GO exposure.

DOI: 10.1021/acsnano.6b00130
ACS Nano 2016, 10, 4459−4471

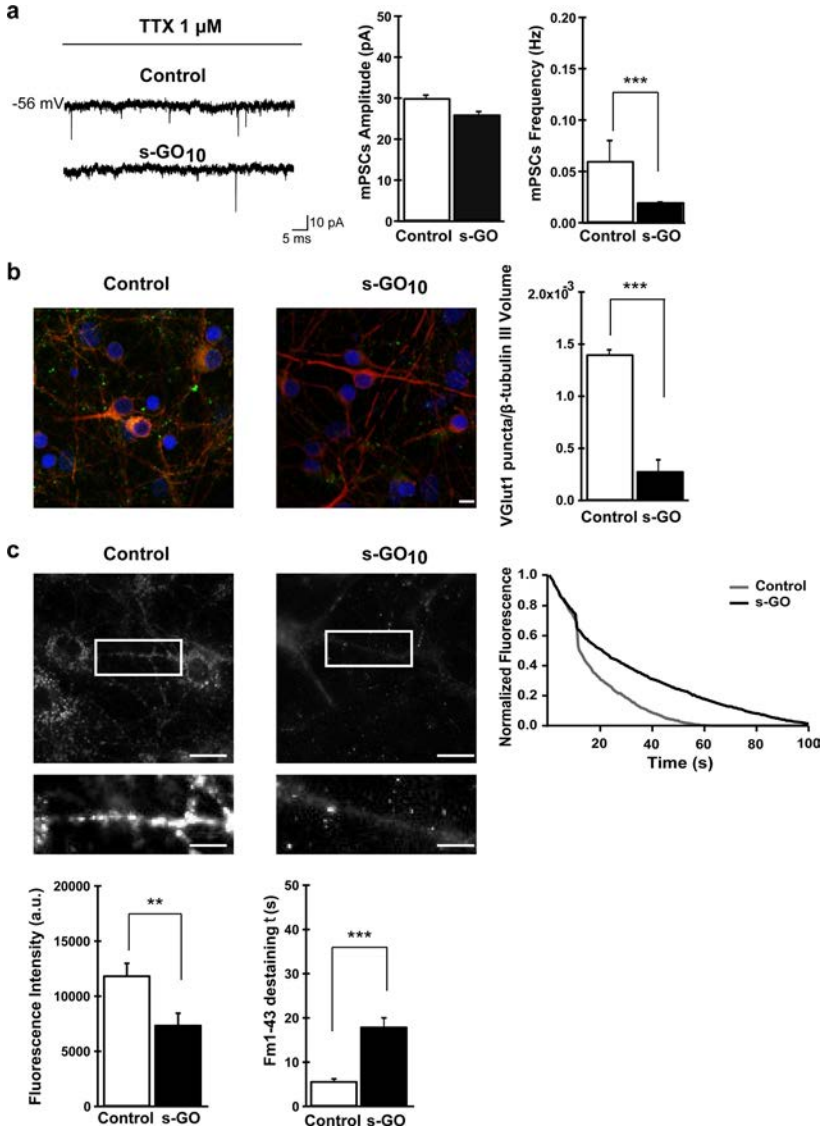

Figure 3. s-GO exposure at high concentration impaired excitatory synapses. (a) Sample tracings of mPSCs recorded in control and s-GO-treated cultures (left panel). Right panel: plots reporting mPSC amplitude and frequency values. s-GO treatment significantly decreased the frequency of mPSCs (* = $P < 0.001$ Student's t test). (b) Confocal reconstruction of control and s-GO-treated neurons immunolabeled for the vesicular glutamate transporter 1 (VGLUT1, green) and counterstained for cytoskeletal component β- tubulin III (red; nuclei are visualized by DAPI in blue; scale bar 10 μm). The plot shows the significant decrease of VGLUT1-positive puncta in s-GO-treated cultures (*** = $P < 0.001$ Student's t test). (c) Top: fluorescence images following staining with FM1-43, control, and s-GO-treated. Scale bar 50 μm. The areas in the boxes are higher magnifications to highlight the difference in vesicular staining between the two conditions (scale bar 100 μm). The plot (top right) reproduces the representative (control and s-GO) traces of FM1-43 destaining (please note that each trace has been normalized to the maximum fluorescence detected). Bottom: left plot summarizes the initial raw fluorescent intensities of hippocampal terminals from control and s-GO-treated cultures (** = $P < 0.01$ Mann−Whitney test); the right plot summarizes the decay time constant τ of FM1-43 destaining in the two conditions (*** = $P < 0.001$, Mann−Whitney test).**

Next, we recorded single-cell synaptic activity in the presence of TTX (1 μM, Figure 3a). Under these experimental conditions, synaptic currents, termed miniature PSCs (mPSCs), do not depend on action potential generation. mPSCs are due to the stochastic fusion of neurotransmitter vesicles at the presynaptic membrane, and their frequency is proportional to the number of synaptic contacts.[28] Despite the fact that in the recorded hippocampal neurons spontaneous synaptic activity was manifested as inward currents (in our recording conditions, see Methods[21]) made up by a mixed population of inhibitory ($GABA_A$ receptor-mediated) and excitatory (AMPA glutamate receptor-mediated) PSCs, virtually all mPSCs, as previously reported,[22] were identified as excitatory by their fast kinetics (decay time constant $\tau = 4 \pm 0.3$ ms; see Methods[22]). Notably, s-GO significantly decreased ($P < 0.001$, Student's t test; see plots in Figure 3a) the frequency of mPSCs without affecting their amplitude (0.06 ± 0.02 Hz and 30 ± 0.7 pA, control, $n = 15$; 0.02 ± 0.001 Hz and 26 ± 0.7 pA, s-GO-treated, $n = 9$; summarized in Figure 3a). To ascertain whether the s-GO interference with synaptic activity was selective on glutamate-mediated fast synaptic transmission, we tested the occurrence of evoked inhibitory PSCs by pair recordings of monosynaptically coupled neurons[22] (Methods and Figure S6a), and we observed that s-GO apparently did not impair $GABA_A$-mediated connections.

DOI: 10.1021/acsnano.6b00130
ACS Nano 2016, 10, 4459−4471

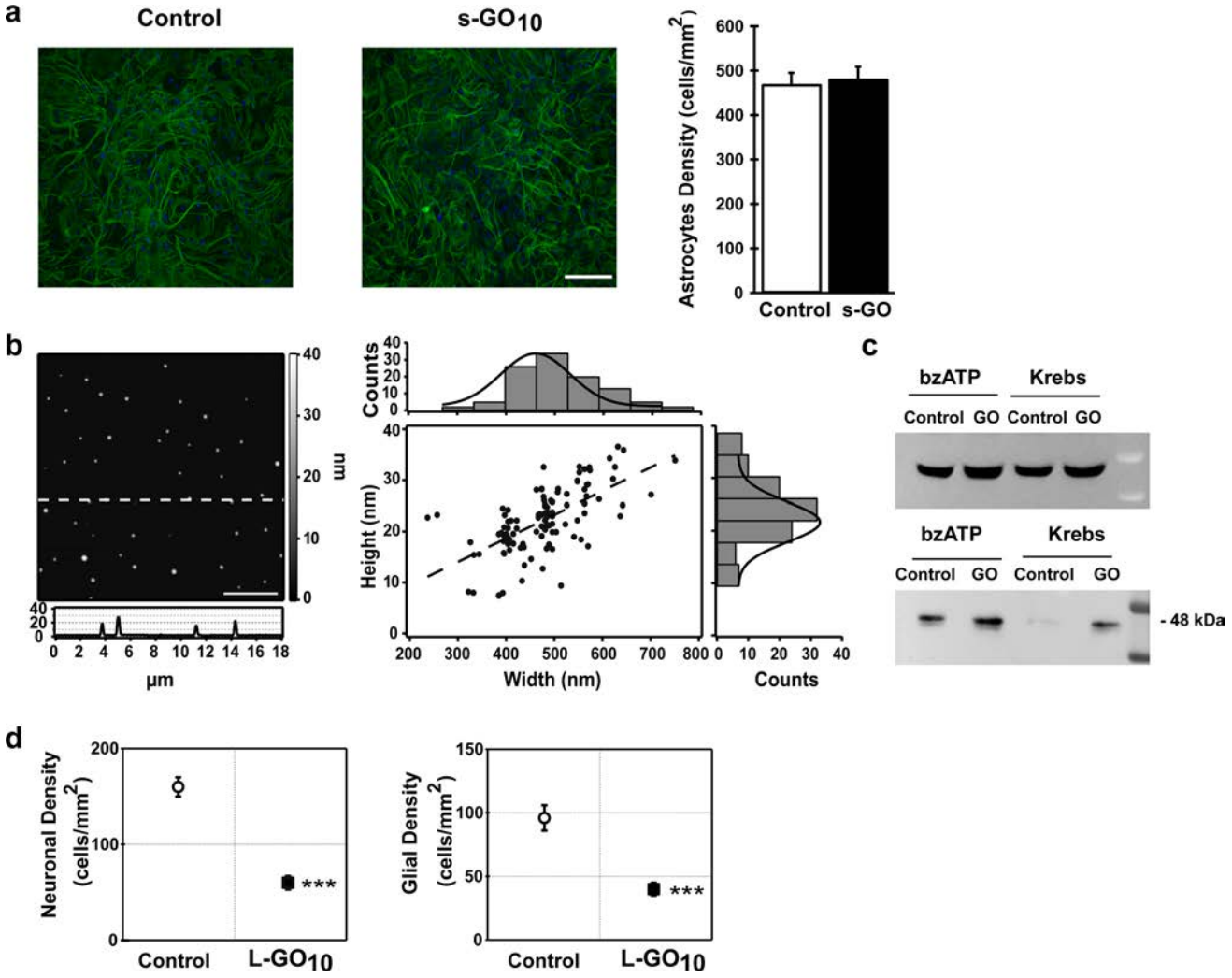

Figure 4. s-GO exposure and microvesicle release in glial cells. (a) Immunolabeling of primary rat astrocytes (3 weeks) in control and s-GO-treated cells (10 μg/mL, 6−8 days). Both cultures were immunostained for GFAP (green) and nuclei visualized by DAPI (blue; scale bar 100 μm). No statistical significance was found between the two conditions (top right). (b) AFM image of fixed MVs, where the differences in color are representative of height differences (brighter means higher). A representative height profile crossing three MVs is reported. The scatter plot (right) shows MV width *versus* height distribution and is fitted with a regression line represented by the equation $y = 0.046x + 0.218$. A frequency histogram, built upon experimental measurements of both width and height, was plotted over each axis of the scatter graph and fitted with Gaussian distributions. The frequency histograms revealed the highest number of occurrences to be about 490 and 24 nm for width and height, respectively. (c) Western blotting of the pellets (bottom row) and cell lysates (top row) for the MV marker flotillin-1. Pellets were obtained from the medium of glial cultures treated or untreated with s-GO under two different conditions: stimulated and not stimulated (Krebs) by 100 μM bzATP. Note the marked increase of the band for flotillin-1 in s-GO-treated cells. (d) Plots summarizing the decreased density of hippocampal cells when treated with l-GO (~10 μm lateral size; 10 μg/mL final concentration).

To determine whether changes in excitatory synaptic density may account for the reduction in fast mPSC frequency detected in s-GO-treated cultures, neurons were co-immunostained for β-tubulin III and the vesicular glutamate transporter (VGLUT1), a transmembrane protein localized at the glutamatergic presynaptic terminals.[29] Antibody to VGLUT1 labeled presynaptic boutons under both conditions (Figure 3b). Using β-tubulin III labeling to identify neuronal bodies and dendrites, we quantified VGLUT1-positive puncta, detecting a significant ($P < 0.001$; Student's t test) reduction in their density in s-GO-treated samples ($1.4 \times 10^{-3} \pm 0.045 \times 10^{-3}$, $n = 6$ fields for control and $0.28 \times 10^{-3} \pm 0.11 \times 10^{-3}$, $n = 6$ fields for s-GO; plot in Figure 3b). Parallel experiments were performed to quantify GABAergic synapses, by similar co-staining but for the vesicular GABA transporter (VGAT) to localize presynaptic GABAergic terminals.[22,30] These studies indicated that s-GO incubation did not alter the inhibitory connection density (Supporting Information and Figure S6b).

In the next set of experiments, we measured the kinetics of synaptic vesicle release by real-time imaging of vesicles labeled with FM dye to monitor the rate of presynaptic vesicle recycling from hippocampal neurons treated or untreated with s-GO. After being stained with the lipophilic dye FM1-43,[31−33] clusters of presynaptic terminals were visible as bright fluorescent spots (Figure 3c). The fluorescence intensity measured on FM-positive puncta following high KCl (50 mM[34]) depolarization is proportional to the number of vesicles endocytosed during synaptic vesicle recycling and thus allows estimation of the size of the recycling vesicle pool.[34] In s-GO-treated cells, upon a high-K^+-loading protocol, we detected a significant ($P < 0.01$; Mann−Whitney test) reduction in the raw fluorescence intensity of FM1-43-positive hippocampal

DOI: 10.1021/acsnano.6b00130
ACS Nano 2016, 10, 4459−4471

terminals (11876 ± 1100 arbitrary units (au), n = 7 fields for control and 7400 ± 1057 au, n = 6 fields for s-GO; three different culture series; Figure 3c), suggesting that chronic incubation with s-GO decreased the recycling vesicle pool. When analyzing the decay time constant (τ) of the FM1-43 fluorescence destaining profiles during vesicle exocytosis, we observed a significant (P < 0.001; Mann−Whitney test) difference in the kinetics displayed by control (τ = 5.7 ± 0.5 s, n = 205 terminals) and s-GO-treated (τ = 18 ± 2 s, n = 85 terminals) cells, as summarized in Figure 3c. In reference experiments, the image series captured on FM1-43-stained cells, but without the high-K^+ destaining stimulus, produced a baseline reference plot (not shown). Taken together, these results support the specific ability of chronic exposure to s-GO flakes to reduce the amount of excitatory synaptic contacts and to interfere with presynaptic vesicle recycling.

To test the ability of s-GO to impair cell membrane dynamics, in general, we investigated whether s-GO (10 μg/mL) was also reducing exocytosis and recycling of synaptic-like microvesicles[15] from cultured primary glial cells (see Methods). MVs are released into the extracellular space by direct budding from the plasma membrane of astrocytes and have been shown to contribute to intercellular communication.[15,35,36] We treated pure glial cell cultures with s-GO (10 μg/mL) for 6−8 days. In Figure 4a, immunofluorescence staining of control and s-GO-treated GFAP-positive cells are shown. s-GO incubation did not affect astrocyte density (Figure 4a, right histograms; n = 20 fields for both conditions), excluding any cytotoxic effect. In glial cultures, MV release was induced by bzATP incubation (100 μM, 30 min, n = 3 different series of cultures[37−39]), and MV release was detected and quantified by immunoblot analysis of the collected supernatant. In control, bzATP stimulation induced the appearance of the band corresponding to flotillin-1 (Figure 4c, bottom blot), a signature of MV release.[40−42] Surprisingly, in s-GO-treated astrocytes, the bzATP stimulation induced a marked increase in the size of the flotillin-1 band. This band was also detected in the absence of stimulation (Figure 4c, bottom blot), suggesting that s-GO *per se* induced the MVs' constitutive release.

AFM micrographs in Figure 4b (left panel) show the presence of vesicles in the stimulated control supernatant appearing as circular spots protruding from the ultraflat mica surface. For each of them, width and height were independently measured from particle crossing height profiles, and the resulting distributions were plotted (Figure 4b, right panel). Intriguingly, similar experiments with GR (10 μg/mL) did not induce shedding of MVs in glial cell cultures (Supporting Information and Figure S7).

We also attempted to investigate the effect of increased lateral size of GO (l-GO, with a lateral dimension in the few micromter range; 10 μg/mL final concentration) on cultured hippocampal cells. However, after 6−8 days of incubation, we measured a significant (P < 0.001; Student's t test; Figure 4d) reduction in both neuron and glial cell densities (160 ± 10 neurons/mm^2 and 96 ± 10 astrocytes/mm^2 for control and 96 ± 10 neurons/mm^2 and 40 ± 7 astrocytes/mm^2 for l-GO; n = 10 visual fields each, three series of cultures; Figure 4d), indicating cell toxicity that prevented any further functional measurements. We believe further investigations are warranted to explore such lateral size-dependent cytotoxic responses.

We report here the ability of s-GO nanosheets to interfere specifically with neuronal synapses, without affecting cell viability. In particular, in cultured neuronal networks, upon chronic s-GO exposure, glutamatergic release sites were sized down. This was shown by (i) the reduction in frequency of spontaneous synaptic activity (PSCs and mPSCs) together with the marked reduction in VGLUT1-positive labeling,[43] (ii) the reduced probability of finding active neurons when networks were explored by Ca^{2+} imaging,[23,44] and (iii) the decreased recycle vesicle pool quantified by FM1-43 measurements together with the altered kinetics of vesicle recycling.[34] This down-regulation of glutamate-mediated synapses was apparently not due to a general cell membrane disruption or to neuronal cell loss. In fact, we never detected alterations in basic electrophysiological parameters, reflecting neuronal health and membrane integrity.[18−20]

In addition, cell densities in treated cultures were comparable to control ones. The survival of GFAP-positive glial cells was also not affected by s-GO exposure, both in mixed neuronal and in pure neuroglial cultures. In the latter condition, MV release was indirectly monitored by the blot analysis of flotillin-1 protein,[40,41] and MV presence was confirmed by direct AFM measures. In these cultures, exposure to s-GO stimulated the basal release of shed vesicles and augmented the bzATP-induced one.[37−39] s-GO increase in MV release from neuroglia cells might be related to a general cell-stress condition[15] ultimately due to s-GO glial−membrane interactions or even internalization, depending on the flakes' shape, lateral dimension, and oxidization degree,[10] as well as the degree of protein adsorption from the culturing milieu.[45]

Based on our experimental evidence, we cannot rule out that treatment with s-GO down-regulated the synaptic function (in particular, presynaptic release) *via* MVs released in mixed neuronal−glial cultures, thus excluding a direct, membrane interference of s-GO nanosheets at the presynaptic glutamatergic terminals. MVs have long been reported as active messengers of intercellular communication, rather than mere inert debris;[37] however, to our knowledge, there are no reports of astrocyte shedding MVs acting as regulators of synaptic activity. On the contrary, MVs released by microglia have been reported to affect synaptic activity, mainly acting at the presynaptic site of the excitatory synapses, but increasing synaptic activity and release in primary cultures.[37] Against this neuroglial cell-mediated response to s-GO is also the fact that astrocyte density in mixed cultures is artificially kept at a low level by the culturing procedure itself, while the surviving microglia are even fewer.[46]

In contrast to s-GO, the inert nature of GR flakes regarding synaptic activity and MV release by glia is also of interest. This could be due to differences in shape and lateral size affecting flake−membrane interactions.[10] It is also interesting to consider that GR has a much less hydrophilic surface characteristic and overall poorer dispersibility in cell culture media[45] that may lead to the formation of aggregates potentially unable to interact with submicroscopic structures (such as the synaptic clefts).

The apparent selectivity in terms of the presynaptic terminals targeted by s-GO was also notable, with the inhibitory GABAergic ones that remained unaffected, as evidenced by pair recordings and the VGAT labeling.[22] Given the ability of graphene flakes to undergo motion and vibration that can lead to interaction with and possible piercing of lipid bilayers,[8] we propose an alternative mechanistic interpretation of our synaptic results. s-GO flakes may prevent the synaptic vesicle endocytotic cycle because their dimensions allow them to interact with the presynaptic cell membrane at the periphery of

DOI: 10.1021/acsnano.6b00130
ACS Nano 2016, 10, 4459−4471

the synaptic cleft and then be taken up by vesicles. In this process, the flakes may transiently trap vesicles in an open mode and prevent their closing and the subsequent endocytosis. This could affect synaptic release in the short term, inducing, in the long term, a down-regulation of glutamatergic release sites and synapses. Note that glutamatergic synaptic activity is specifically, and reversibly, affected also when neurons are transiently exposed to s-GO, with a short-term up-regulation of release, turned into a down-regulation within the first 3 days of chronic exposure (Figure S8 in Supporting Information). This observation further supports the hypothesis of the ability of s-GO to directly target synapses. The mechanism of such interaction among s-GO flakes and vesicles (including extra-synaptic ones) could be similar to what has been previously described for dispersed single-walled carbon nanotubes.[47] In this context, the unlikeliness of affecting GABAergic terminals may reside in the different dimensions of the excitatory (16 nm) and inhibitory (10 nm) synaptic clefts.[48] The latter are reported to be narrowed to 6 nm at the periphery of the clefts due to transcleft elements, while docked vesicles are concentrated at the central cleft domain.[48] On the contrary, docked vesicles in excitatory synapses are distributed evenly over the synaptic cleft.[48] It is tempting to speculate that these synaptic ultrastructural differences might explain why glutamatergic terminals became ideal targets of s-GO interactions. This selectivity is supported by the notion that, even when transiently exposed to s-GO *via* pressure-ejected brief pulses, GABAergic synapses are unaffected (see Supporting Information and Figure S8).

CONCLUSIONS

Regardless of the mechanisms involved, the described ability of s-GO to alter synapses and induce glial cell reaction has not been previously documented. This might compromise neuronal signaling and CNS functions and seems crucially dependent on the GO sheet dimensions since larger flakes were found unequivocally cytotoxic. In our experiments, 6 days of exposure of cultures to equal amounts of dispersed l-GO induced unequivocal hippocampal cell loss, both neuroglia and neurons, thus hampering any further evaluation of membrane/flake interactions.

These observations deserve further studies; in fact, altering synapses and inducing glia reactivity may raise concerns from a safety and nanotoxicity point of view.[49]

Beyond the safe design of nanomaterials, such a subtle interference affecting exquisite CNS signaling may offer possibilities in neuropharmacology when specific targeting of excitatory synapses is desired.[50−52] The use of nanoparticles as therapeutics is, in fact, fueled by their ability to circumvent biological barriers,[53] and targeting of synapses has created the basis for theranostics applications.[54] Our observations with thin s-GO flakes illustrate the potential of 2D nanosheet physical properties to engineer specific glutamate transmission modulators.

It is also relevant to note that synapse formation and function in neuronal networks, when interfaced to planar graphene-based materials, are not affected.[55] This strengthens the notion that when exploring the application of graphene in biology, studies should be performed with well-characterized types of materials because the materials' physical−chemical features, including geometry, are governing the potential interactions with specific biological components.[2]

METHODS

Synthesis and Characterization of Biological-Grade Thin Graphene Oxide of Different Lateral Size Distribution. For graphene oxide preparation, graphite flakes (Graflake 9580) were obtained from Nacional Grafite Ltd. (Brazil) and used for the preparation of large and small graphene oxide. Nitric acid 70%, sodium nitrate, potassium permanganate, sulfuric acid 99.999%, and hydrogen peroxide 30% were purchased from Sigma-Aldrich. Water for injection was obtained from Fresenius Kabi.

Graphene oxide sheets were synthesized using the modified Hummers method previously described[56] and under endotoxin-free conditions by using a laminar flow hood, water for injection, gloves, nonpyrogenic plastic containers, and depyrogenated glassware.[57] Briefly, 0.8 g of graphite flakes was mixed with 0.4 g of sodium nitrate in a round-bottom flask, and then 18.4 mL of sulfuric acid 99.999% was added slowly to the mixture. After a homogenized mixture was obtained, 2.4 g of potassium permanganate was slowly added and the mixture was maintained for 30 min. Next, 37 mL of water for injection was added dropwise due to the violent exothermic reaction, and the temperature was continuously monitored and kept at 98 °C for 30 min. The mixture was further diluted with 112 mL of water for injection, and 30% hydrogen peroxide was added for the reduction of the residual potassium permanganate, manganese dioxide, and manganese heptoxide to soluble manganese sulfate salts. The resulting mixture was purified by several centrifugation steps at 9000 rpm for 20 min until a viscous orange/brown layer of pure GO started to appear on top of the oxidation byproducts at neutral pH.[58]

This GO gel-like layer was extracted carefully with warm water, resulting in the large GO. Final concentrations ranging between 1 and 2 mg/mL were obtained with a yield of *ca.* 10%. l-GO was freeze-dried, reconstituted in water for injection, sonicated in a bath sonicator (VWR, 80W) for 5 min, and centrifuged at 13 000 rpm for 5 min at room temperature to prepare the s-GO. Structural properties such as lateral dimension and thickness of the GO materials have been studied by optical microscopy, TEM, and AFM. Optical properties such as absorbance and fluorescence have been studied by using UV−vis and fluorescence spectroscopy, respectively. Surface properties have also been studied by Raman spectroscopy and ζ-potential measurements. To elucidate the functionalization degree of the GO sheets, TGA was performed. X-ray photoelectron spectroscopy has been used to quantify the chemical composition of the GO sheets, C/O ratio, and the contribution of each individual functional group such as carboxylic, carbonyl, and epoxides.

Optical Microscopy. Bright-field microscopy using a Zeiss Primovert microscope was used to assess the lateral dimension distribution of the l-GO and to verify the size reduction of the s-GO.

Transmission Electron Microscopy. TEM was performed using a FEI Tecnai 12 Biotwin microscope (FEI, The Netherlands) at an acceleration voltage of 100 kV. Images were taken with Gatan Orius SC1000 CCD camera (GATAN, UK). One drop of sample was placed on a Formvar/carbon-coated copper grid. Filter paper was used to remove the excess material.

Atomic Force Microscopy. A multimode AFM was used on the tapping-mode with a J-type scanner, Nanoscope V8 controller (Veeco, Cambridge, UK), and an OTESPA silicon probe (Bruker, UK). Images were taken in air by depositing 20 μL of 100 μg/mL of GO on a freshly cleaved mica surface (Agar Scientific, Essex, UK) coated with poly-L-lysine 0.01% (Sigma-Aldrich, UK) and allowed to adsorb for 5 min. Excess unbound material was removed by washing with Milli-Q water and then allowed to dry in air; this step was repeated once. Lateral dimension and thickness distributions of GO were carried out using NanoScope Analysis software (version 1.40 Bruker, UK).

UV/Visible Spectroscopy. UV/visible absorbance spectra were obtained for GO samples from 7.5 to 20 μg/mL using a Varian Cary winUV 50 Bio spectrophotometer. Dual beam mode and baseline correction were used throughout the measurements to scan the peak wavelength and maximum absorbance between 200 and 800 nm.

Fluorescence Spectroscopy. Fluorescence emission spectroscopy was performed for GO samples from 75 to 200 μg/mL using a LS-50B

DOI: 10.1021/acsnano.6b00130
ACS Nano 2016, 10, 4459−4471

PerkinElmer spectrofluorimeter at the excitation wavelength of 525 nm, with both excitation and emission slits set at 20.

Raman Spectroscopy. Raman spectra were recorded for GO (20 μL of 100 μg/mL) on glass slides after complete evaporation of the water. Measurements were carried out using a 50× objective at 633 nm laser excitation using a micro-Raman spectrometer (ThermoScientific, UK). An average of five different locations within each sample was measured to calculate the I_D/I_G ratio.

Zeta-Potential Measurements. Electrophoretic mobility (μ) was measured by Malvern Zetasizer Nano ZS (UK) after dilution of samples with water in disposable Zetasizer cuvettes (Malvern Instruments). Default instrument settings and automatic analysis were used for all measurements, where the μ was converted automatically by the equipment software to zeta-potential (ζ) values as it is directly related to ζ-potential by Henry's equation. All values for samples prepared are triplicate measurements, and values were mean ± SD.

Thermogravimetric Analysis. The weight loss of GO samples was performed by TGA using a Pyris 6, PerkinElmer Ltd. GO (1−2 mg) was weighed into a ceramic crucible and analyzed from 100 to 995 °C at 10 °C/min with a nitrogen flow of 20 mL/min.

X-ray Photoelectron Spectroscopy. The composition of GO surfaces was studied by XPS at the NEXUS facility (the UK's National EPSRC XPS Users' Service, hosted by nanoLAB in Newcastle-upon-Tyne). XPS was recorded using a Thermo Theta Probe XPS spectrometer with a monochromatic Al Kα source of 1486.68 eV. The survey XPS spectra were acquired with pass energy (PE) of 200 eV, 1 eV step size, 50 ms dwell time, and averaged over five scans. The etching was 90 s. High-resolution C 1s XPS spectra were acquired with PE of 40 eV, 0.1 eV step size, 100 ms dwell time, and averaged over 20 scans. Spectra from insulating samples have been charge-corrected by shifting all peaks to the adventitious carbon C 1s spectral component binding energy set to 284.6 eV. CasaXPS software was used to process the spectra acquired at NEXUS. For the deconvolution of the different components, the CasaXPS software was used and the different regions were assigned according to NIST's XPS and lasurface databases:

$\pi-\pi^*$: 290.9−289.7
O−C═O: 288.8−288.0 eV
C═O: 287.6−286.6 eV
C−O−C: 286.7−286.3 eV
C−OH: 285.9−285.3 eV
C−C and C═C: 284.6 eV

For graphite samples, the CasaXPS software was able to properly fit the hydroxyl component at 285.6 eV, but for graphene oxide samples, it was not possible to fit six components where we should expect to have the epoxide and hydroxyl contributions separately. The amount of hydroxyls in the graphene oxide samples depends on the degree of oxidation, with the hydroxyl groups being the least oxidized, followed by epoxide, carbonyl, and carboxylic groups (the latter being the most oxidized).

Synthesis and Characterization of Pristine Graphene. The pristine graphene flakes used in this study were obtained by a methodology[16] that uses mechanochemical activation by ball-milling to exfoliate graphite through interactions with melamine (2,4,6-triamine-1,3,5-triazine) in solvent-free conditions. In a typical experiment, 7.5 mg of graphite (purchased from Bay Carbon, Inc. SP-1 graphite powder) and 0.16 mmol of melamine were ball-milled in a Retch PM100 planetary mill at 100 rpm for 30 min in air atmosphere. The resulting solid mixtures were dispersed in 20 mL of water to produce stable black suspensions. The as-prepared dispersions can be filtered and washed in hot water to remove melamine. Graphene water dispersions were obtained with a final concentration of 0.09 mg/mL in Milli-Q water. Melamine traces in the dispersions were analyzed by elemental analysis (LECO CHNS-932, model no. 601-800-500), giving 0.9 ppm of melamine. For TEM analyses, water dispersions were placed on a copper grid (3.00 mm, 200 mesh, coated with carbon film), and samples were investigated by high-resolution transmission electron microscopy (HRTEM) on a JEOL 2100. Lateral dimension distribution was carried out using Fiji-win32. UV−vis−NIR absorbance was performed for GR samples from 2.4 to 14.2 μg/mL using a 1 cm quartz cuvettes on a Cary 5000 UV−vis−NIR spectrophotometer. For Raman spectroscopy, the water dispersions are drop-cast onto a silicon surface (Si-Mat silicon wafers, CZ). Measurements were carried out using a 100× objective at 532 nm laser excitation using a SENTERRA Raman microscope. An average I_D/I_G ratio was measured from different locations in the sample. Thermogravimetric analyses were performed with a TGA Q50 (TA Instruments) at 10 °C/min in a nitrogen atmosphere.

Commercially Sourced Graphene Oxide. The graphene oxide was prepared by stirring powdered carbon fibers (GANF helical-ribbon carbon nanofibers manufactured by the Grupo Antolin Ingeniería, GANF) and sodium nitrate in sulfuric acid at 0 °C. While vigorous agitation was maintained, potassium permanganate was added to the suspension. After 30 min, water was slowly stirred into the paste. Then, the suspension was filtered and rinsed with copious amounts of water to remove the presence of acids.[59] For TEM analyses, water dispersions were placed on a copper grid (3.00 mm, 200 mesh, coated with carbon film). Samples were investigated by HRTEM on a JEOL 2100. Lateral dimension distribution was carried out using Fiji-win32. UV−vis−NIR absorbance was performed for GO samples from 7.5 to 20 μg/mL using a 1 cm quartz cuvettes on a Cary 5000 UV−vis−NIR spectrophotometer. For Raman spectroscopy, the water dispersions were drop-cast onto a silicon surface (Si-Mat silicon wafers, CZ). Measurements were carried out using a 100× objective at 532 nm laser excitation using a SENTERRA Raman microscope. An average I_D/I_G ratio was measured from different locations in the sample. The thermogravimetric analyses were performed with a TGA Q50 (TA Instruments) at 10 °C/min in a nitrogen atmosphere.

Preparation of Primary Cultures. Primary hippocampal cultures were prepared from 2 to 3 days postnatal (P_2-P_3) rats as previously reported.[21,22,60] All procedures were approved by the local veterinary authorities and performed in accordance with the Italian law (decree 116/92) and the UE guidelines (86/609/CE, 2007/526/CE, and 2010/63/UE). The animal use was approved by the Italian Ministry of Health. All efforts were made to minimize suffering and to reduce the number of animals used. All chemicals were purchased by Sigma unless stated otherwise. Briefly, enzymatically dissociated hippocampal neurons[21,22,60] were plated on poly-L-ornithine-coated glass coverslips (Kindler, EU) at a density of 200 000 ± 16 000 cells/mL (measure by sampling n = 4 culture series). Cultures were incubated (37 °C, 5% CO_2) in medium consisting of either 1× MEM (Gibco) or 10× MEM (Gibco) to compensate the volume of the added GR and GO water dispersion when treating cells at higher flakes concentrations (*i.e.*, 10 μg/mL). In both cases, the MEM was supplemented to reach 35 mM glucose, 1 mM Apo-transferrin, 15 mM HEPES, 48 μM insulin, 3 μM biotin, 1 mM vitamin B12, 500 nM gentamicin, and 10% fetal bovine serum (FBS; Invitrogen). For experiments involving chronic treatments, cultures were incubated at 2 DIV, with a medium containing 1 or 10 μg/mL of GR, either s-GO and A-GO, or l-GO, and controls were subjected to the same medium changes with addition of equivalent volumes of Milli-Q water or melamine alone. Cultures were used at days 8−10 (after 6−8 days of incubation).

Primary cortical glial cultures were prepared from P_2-P_3 rats as described in Calegari *et al.*[61] Briefly, dissociated cells were plated into plastic 75 cm^2 flasks, incubated (37 °C; 5% CO_2) in culture medium consisting of DMEM (Gibco), supplemented with 10% FBS, 100 IU/mL penicillin, and 10 mg/mL streptomycin. At 21 DIV, GR or s-GO (10 μg/mL) was added to the culture medium and cultures were used after 6−8 days of incubation.

Electrophysiological Recordings. Single and paired whole-cell recordings were obtained at room temperature (RT) with pipettes (5−7 MΩ) containing (in mM) 120 K gluconate, 20 KCl, 10 HEPES, 10 EGTA, 2 $MgCl_2$, 2 Na_2ATP, pH 7.3; osmolarity was adjusted to 300 mOsm. The extracellular solution contained (in mM) 150 NaCl, 4 KCl, 1 $MgCl_2$, 2 $CaCl_2$, 1 $MgCl_2$, 10 HEPES, 10 glucose (all Sigma), pH 7.4. Coverslips with cultures were positioned in a Perspex chamber mounted on an inverted microscope (Eclipse TE-200, Nikon, Japan). Data were collected by Multiclamp 700B patch amplifier (Axon CNS, Molecular Devices) and digitized at 10 kHz with the pClamp 10.2

DOI: 10.1021/acsnano.6b00130
ACS Nano 2016, 10, 4459−4471

acquisition software (Molecular Devices LLC, USA). The spontaneous synaptic activity was recorded by clamping the membrane voltage at −56 mV holding potential (not corrected for liquid junction potential, which was 14 mV). In paired recordings, the presynaptic neuron was held under current clamp mode at −70 mV (≤0.02 nA negative current injection), and action potentials were elicited by injecting short (4 ms) square current pulses (1 nA). The postsynaptic cell was voltage clamped usually at −56 mV holding potential. Monosynaptic connections were recognized by their short latency (<5 ms[62]), measured between the peak of the evoked action potential and the onset of the postsynaptic current response. All recorded events were analyzed offline with the AxoGraph 1.4.4 (Axon Instrument) event detection software (Axon CNS, Molecular Devices).

Calcium Imaging. Cultures were loaded for 1 h at RT with cell-permeable Fura-2-AM (2 μM) in the extracellular recording solution supplemented with 0.5% bovine serum albumin. The Fura-2-loaded cultures were observed with a 40× objective (0.6 NA, Nikon, Japan), and recordings were performed from visual fields (120 × 160 μm^2) containing on average 7 ± 2 neurons. Prior to recording Ca^{2+} signals, we selected the cells by drawing regions of interest (ROI) around their bodies to reduce any background.[23] Samples were excited at wavelengths of 340 and 380 nm generated by a monochromator device equipped with integrated light source (Polychrome IV, Till Photonics). Excitation light was separated from the light emitted from the sample using a 395 nm dichroic mirror. Images of emitted fluorescence >510 nm were acquired continuously for a maximum of 2400 s (200 ms individual exposure time) by a cooled slow-scan interline transfer camera (IMAGO CCD camera; Till Photonics). The camera was operated on 8 × 8 pixel binning mode, and the imaging system was controlled by an integrating imaging software package (TILLvisION; Till Photonics). To induce rhythmic bursts, 20 μM bicuculline methiodide was bath-applied after 15 min recording;[23] at the end of each experiment, tetrodotoxin (1 μM; Latoxan) was applied to confirm the neuronal nature of the recorded signals.[23] Recorded images were analyzed offline by Clampfit software (pClamp suite, 10.2 version; Molecular Devices LLC, US) and Igor Pro software (6.32A version; WaveMetrics, Lake Oswego, Oregon, USA). Intracellular Ca^{2+} transients were expressed as fractional amplitude increase ($\Delta F/F_0$, where F_0 is the baseline fluorescence level and ΔF is the rise over the baseline); elevations in calcium level were considered significant if they exceeded 5 times the standard deviation of the noise. We then computed the difference between consecutive onset times to obtain the IEI. Hence, after the IEI values were obtained from each active cell in the field, data were pooled for all fields recorded under the same experimental conditions and averaged for further comparison.

FM1-43 Loading and Destaining. Depolarization-dependent staining of synaptic terminals with the styryl dye *N*-(3-triethylammoniumpropyl)-4-(4-(dibutylamino)styryl)pyridinium dibromide (FM1-43, Molecular Probes, Life Technology) was obtained by incubating cultures (after 10 min saline buffer wash at RT) for 120 s with 50 mM KCl and FM1-43 (15 μM). The buffer was replaced with 2 mL of normal saline containing FM1-43, and cells were left to recover for 10 min to ensure complete recycling of the vesicles[63] and then incubated for 10 min with saline containing 6-cyano-7-nitroquinoxaline-2,3-dione (10 μM) and 2-aminophosphonovaleric acid (50 μM) to prevent network activity altering the rate of FM release. These antagonists were present throughout the experiment. After incubation with FM1-43 dye, cultures were transferred to the stage of a Nikon Eclipse Ti−U inverted microscope equipped with a piezoelectric table (Nano-ZI Series 500 μm range, Mad City Laboratories), HBO 103 W/2 mercury short lamp (Osram, Munich, Germany), mirror unit (exciter filter BP 465−495 nm, dichroic 505 nm, emission filter BP 515−555), and electron multiplier CCD camera C9100-13 (Hamamatsu Photonics, Japan). Images were acquired with an oil-immersion Plan Apo 100× (1.4 NA, Nikon, Japan) objective at a sampling of 2 Hz with a spatial resolution of 256 × 256 pixels. All experiments were performed at RT. Application of 50 mM KCl (5 s), followed by a 2 min washout, was used to stimulate vesicle exocytosis from the dye-containing terminals, measured as a fluorescence loss. The imaging system was controlled by an integrating imaging software package (NIS Element, Nikon, Japan). Offline analysis was performed on the image sequence with the image-processing package Fiji.[64] After background subtraction, images were analyzed using rounded ROIs of 4 pixels in diameter drawn on neural processes. Endocytosed vesicles during FM1-43 loading were measured by estimating the brightness of the total vesicle pool puncta (raw fluorescence intensity) in GO-treated and untreated cultures before the unloading stimulus. The decay time constant, τ, was measured by pClamp 10.2 software (Molecular Devices LLC, USA). To avoid imaging nonselective FM staining, only puncta that showed stimulus-dependent destaining were included in the analyses.

Immunofluorescence Labeling. Hippocampal neurons or glial cells, treated and untreated, were fixed in PBS containing 4% PFA for 20 min at RT. Cells were permeabilized with 1% Triton X-100 for 30 min, blocked with 5% FBS in PBS for 30 min at RT, and incubated with primary antibodies for 30 min. The primary antibodies used were rabbit polyclonal anti-β-tubulin III (Sigma T2200, 1:250 dilution), mouse monoclonal anti-GFAP (Sigma-Aldrich, 1:500 dilution), and guinea pig polyclonal antivesicular glutamate transporter (Millipore AB5905, dilution 1:2000). After the primary incubation and PBS washes, neurons were incubated for 30 min with the secondary antibodies AlexaFluor 594 goat anti-rabbit (Invitrogen, dilution 1:500), AlexaFluor 488 goat anti-mouse (Invitrogen, dilution 1:500), AlexaFluor 488 goat anti-guinea pig (Invitrogen, dilution 1:500), and DAPI (Invitrogen, dilution 1:200) to stain the nuclei. Samples were mounted in Vectashield (Vector Laboratories) on 1 mm thick coverslips. Cell densities were quantified at 20× (0.5 NA) magnification using a DM6000 Leica microscope (Leica Microsystems GmbH, Wetzlar, Germany), with random sampling of seven to ten fields (713 × 532 μm; control and treated, n = 3 culture series). For VGLUT1-positive terminals, image acquisition was performed using a confocal microscope (Leica Microsystems GmbH, Wetzlar, Germany) with 63× (1.4 NA) magnification (*Z*-stacks were acquired every 300 nm; 12 fields for control and untreated conditions). Offline analysis was performed using Volocity software (Volocity 3D image analysis software, PerkinElmer, USA). For each set of experiments, the images were acquired using identical exposure settings. The ROIs for the quantification were blindly chosen using the tubulin channel. For each analyzed field, we used the *Z*-stacks to quantify VGLUT1 puncta as 3D objects. The resulting numbers were normalized to the relative cellular volume calculated on the basis of β-tubulin III labeling.

Micovesicle Isolation and Characterization. Microvesicle shedding was induced in 21 DIV confluent glial cells (after washing in PBS, 37 °C) upon exposure to benzoyl-ATP (bzATP; 100 μM) in Krebs−Ringer solution with the following composition: 125 mM NaCl, 5 mM KCl, 1.2 mM $MgSO_4$, 1.2 mM KH_2PO_4, 2 mM $CaCl_2$, 6 mM D-glucose, and 25 mM HEPES/NaOH (pH adjusted to 7.4), for 30 min at 37 °C and 5% CO_2.[39] MVs were pelleted by centrifugation as described in Bianco *et al.*[39] Negative controls were incubated with Krebs−Ringer solution without the presence of bzATP. MVs isolated from confluent mixed glial cells were resuspended in lysis buffer (50 mM Tris-HCl, pH 8.0, 150 mM NaCl, 1% NP40, 0.1% SDS), sonicated 3 × 10 s, and then boiled at 95 °C for 5 min. Samples were run on a 10% polyacrylamide gel and were blotted onto nitrocellulose filters (Millipore, Italy). Filters were then blocked in PBS-Tween-20 (0.1%) plus 5% nonfat dry milk and incubated with the primary antibody antiflotillin-1 (dilution 1:1000) for 16 h at 4 °C. Specific MV marker flotillin-1[40,41] was detected with mouse monoclonal anti-flotillin-1 (dilution 1:1000). After three washes with PBS-Tween, filters were incubated with peroxidase-conjugated anti-mouse secondary antibody (dilution 1:1000). Optical density of immunolabeled ECL-exposed protein bands was measured with UVI-1D software.

For the AFM characterization, MVs were diluted 1:10 in PBS buffer solution and processed as described in Junker *et al.*[65] Briefly, a 15 μL drop of sample solution was placed and left to adsorb (15 min) onto a freshly peeled mica substrate, thereafter rinsed with PBS. In order to reduce vesicle collapsing during AFM analysis, vesicles were fixed with 1% formaldehyde for 1 h (RT). MVs were then washed with PBS and dried under a gentle stream of nitrogen. AFM was used in semicontact mode at RT in air using a commercial instrument (Solver Pro, NT-MDT, RU). Silicon tips (NSC36/CR-AU, MikroMash, USA) with a

DOI: 10.1021/acsnano.6b00130
ACS Nano 2016, 10, 4459−4471

typical force constant of 0.6 nN/nm and a resonance frequency of about 65 kHz were employed. Topographic height and phase images were recorded at 512 × 512 pixels at a scan rate of 0.5 Hz. Image processing was performed using Gwyddion freeware AFM analysis software, version 2.40.[66] For statistical analysis, 107 individual MVs were imaged in seven different fields and measured. In particular, width and height of each vesicle were evaluated from cross-line profiles, and results were statistically analyzed using Igor Pro software (Wavemetrics. USA).

ASSOCIATED CONTENT

Supporting Information

The Supporting Information is available free of charge on the ACS Publications website at DOI: 10.1021/acsnano.6b00130.

Supporting results, Figures S1−S8, and Tables S1 and S2 (PDF)

AUTHOR INFORMATION

Corresponding Authors

*E-mail: prato@units.it.

*E-mail: laura.ballerini@sissa.it.

Author Contributions

R.R. and A.F. performed cell biology, electrophysiology, and immunofluorescence experiments and analysis; R.R. and F.P.U.S. designed and performed imaging and real-time imaging experiments and analysis; N.L. and K.K. contributed to the synthesis and characterization of thin graphene oxide (l-GO and s-GO) of biological grade; V.L. and E.V. contributed to the synthesis and characterization of pristine graphene; M.M. performed glial cell experiments, immunofluorescence, and Western blot; D.S., I.R., and L.C. designed and performed the AFM experiments; L.B. and M.P. conceived the study; L.B. conceived the experimental design and contributed to the analysis of data; L.B. wrote the manuscript.

Notes

The authors declare no competing financial interest.

ACKNOWLEDGMENTS

We are especially grateful to Micaela Grandolfo, Jessica Franzot, and Beatrice Pastore for supervising the synaptic immune staining and quantification, the glial cell culturing, and Western Blot experiments. IOM-TASC National Laboratory (Trieste) is also gratefully acknowledged for AFM assistance. N.L. acknowledges Leon Newman for assistance with the TEM and Raman instrumentation. The authors acknowledge the staff in the Faculty of Life Sciences EM Facility and the Wellcome Trust for equipment grant support to the EM Facility. The University of Manchester Bioimaging Facility microscopes used in this study were purchased with grants from the BBSRC, Wellcome Trust, and the University of Manchester Strategic Fund. X-ray photoelectron spectroscopy was performed at the National EPSRC XPS User's Service (NEXUS) at Newcastle University, an EPSRC Mid-Range Facility. The Antolin group is also acknowledged for the provision of the commercial material. We acknowledge financial support from the EU FP7-ICT-2013-FET-F GRAPHENE Flagship project (No. 604391) from the NEUROSCAFFOLDS-FP7-NMP-604263 and PRIN-MIUR No. 2012MYESZW.

REFERENCES

(1) Sanchez, V. C.; Jachak, A.; Hurt, R. H.; Kane, A. B. Biological Interactions of Graphene-Family Nanomaterials: An Interdisciplinary Review. *Chem. Res. Toxicol.* **2012**, *25*, 15−34.

(2) Kostarelos, K.; Novoselov, K. S. Materials Science. Exploring the Interface of Graphene and Biology. *Science* **2014**, *344*, 261−263.

(3) Mao, H. Y.; Laurent, S.; Chen, W.; Akhavan, O.; Imani, M.; Ashkarran, A. A.; Mahmoudi, M. Graphene: Promises, Facts, Opportunities, and Challenges in Nanomedicine. *Chem. Rev.* **2013**, *113*, 3407−3424.

(4) Bitounis, D.; Ali-Boucetta, H.; Hong, B. H.; Min, D. H.; Kostarelos, K. Prospects and Challenges of Graphene in Biomedical Applications. *Adv. Mater.* **2013**, *25*, 2258−2268.

(5) Krishna, K. V.; Ménard-Moyon, C.; Verma, S.; Bianco, A. Graphene-Based Nanomaterials for Nanobiotechnology and Biomedical Applications. *Nanomedicine (London, U. K.)* **2013**, *8*, 1669−1688.

(6) Wang, Y.; Li, Z.; Wang, J.; Li, J.; Lin, Y. Graphene and Graphene Oxide: Biofunctionalization and Applications in Biotechnology. *Trends Biotechnol.* **2011**, *29*, 205−212.

(7) Kuzum, D.; Takano, H.; Shim, E.; Reed, J. C.; Juul, H.; Richardson, A. G.; de Vries, J.; Bink, H.; Dichter, M. A.; Lucas, T. H.; Coulter, D. A.; Cubukcu, E.; Litt, B. Transparent and Flexible Low Noise Graphene Electrodes for Simultaneous Electrophysiology and Neuroimaging. *Nat. Commun.* **2015**, *5*, 5259−5263.

(8) Li, Y.; Yuan, H.; von dem Bussche, A.; Creighton, M.; Hurt, R. H.; Kane, A. B.; Gao, H. Graphene Microsheets Enter Cells Through Spontaneous Membrane Penetration at Edge Asperities and Corner Sites. *Proc. Natl. Acad. Sci. U. S. A.* **2013**, *110*, 12295−12300.

(9) Tu, Y.; Lv, M.; Xiu, P.; Huynh, T.; Zhang, M.; Castelli, M.; Liu, Z.; Huang, Q.; Fan, C.; Fang, H.; Zhou, R. Destructive Extraction of Phospholipids from Escherichia Coli Membranes by Graphene Nanosheets. *Nat. Nanotechnol.* **2013**, *8*, 594−601.

(10) Mao, J.; Guo, R.; Yan, L. Simulations and Analysis of Cellular Internalization Pathways and Membrane Perturbation for Graphene Nanosheets. *Biomaterials* **2014**, *35*, 6069−6077.

(11) Rizzoli, S. O. Synaptic Vesicle Recycling: Steps and Principles. *EMBO J.* **2014**, *33*, 788−822.

(12) Bianco, A. Graphene: Safe or Toxic? The Two Faces of the Medal. *Angew. Chem., Int. Ed.* **2013**, *52*, 4986−4997.

(13) Yang, D.; Li, T.; Xu, M.; Gao, F.; Yang, J.; Yang, Z.; Le, W. Graphene Oxide Promotes the Differentiation of Mouse Embryonic Stem Cells to Dopamine Neurons. *Nanomedicine (London, U. K.)* **2014**, *9*, 2445−2455.

(14) Zhang, Y.; Ali, S. F.; Dervishi, E.; Xu, Y.; Li, Z.; Casciano, D.; Biris, A. S. Cytotoxicity Effects of Graphene and Single-Wall Carbon Nanotubes in Neural Phaeochromocytoma-Derived PC12 Cells. *ACS Nano* **2010**, *4*, 3181−3186.

(15) Falchi, A. M.; Sogos, V.; Saba, F.; Piras, M.; Congiu, T.; Piludu, M. Astrocytes Shed Large Membrane Vesicles that Contain Mitochondria, Lipid Doplets and ATP. *Histochem. Cell Biol.* **2013**, *139*, 221−231.

(16) León, V.; Quintana, M.; Herrero, M. A.; Fierro, J. L.; de la Hoz, A.; Prato, M.; Vázquez, E. Few-Layer Graphenes from Ball-Milling of Graphite with Melamine. *Chem. Commun. (Cambridge, U. K.)* **2011**, *47*, 10936−10938.

(17) León, V.; Rodriguez, A. M.; Prieto, P.; Prato, M.; Vázquez, E. Exfoliation of Graphite with Triazine Derivatives under Ball-Milling Conditions: Preparation of Few-Layer Graphene *via* Selective Noncovalent Interactions. *ACS Nano* **2014**, *8*, 563−571.

(18) Carp, J. S. Physiological Properties of Primate Lumbar Motoneurons. *J. Neurophysiol.* **1992**, *68*, 1121−1132.

(19) Gao, Y.; Liu, L.; Li, Q.; Wang, Y. Differential Alterations in the Morphology and Electrophysiology of Layer II Pyramidal Cells in the Primary Visual Cortex of a Mouse Model Prenatally Exposed to LPS. *Neurosci. Lett.* **2015**, *591*, 138−143.

(20) Djuric, U.; Cheung, A. Y.; Zhang, W.; Mok, R. S.; Lai, W.; Piekna, A.; Hendry, J. A.; Ross, P. J.; Pasceri, P.; Kim, D. S.; Salter, M. W.; Ellis, J. MECP2e1 Isoform Mutation Affects the Form and Function of Neurons Derived from Rett Syndrome Patient iPS Cells. *Neurobiol. Dis.* **2015**, *76*, 37−45.

(21) Lovat, V.; Pantarotto, D.; Lagostena, L.; Cacciari, B.; Grandolfo, M.; Righi, M.; Spalluto, G.; Prato, M.; Ballerini, L. Carbon Nanotube

DOI: 10.1021/acsnano.6b00130
ACS Nano 2016, 10, 4459−4471

Substrates Boost Neuronal Electrical Signaling. *Nano Lett.* **2005**, *5*, 1107−1110.
(22) Cellot, G.; Toma, F. M.; Varley, Z. K.; Laishram, J.; Villari, A.; Quintana, M.; Cipollone, S.; Prato, M.; Ballerini, L. Carbon Nanotube Scaffolds Tune Synaptic Strenght in Cultured Neural Circuits: Novel Frontiers in Nanomaterials-Tissue Interactions. *J. Neurosci.* **2011**, *31*, 12945−12953.
(23) Bosi, S.; Rauti, R.; Laishram, J.; Turco, A.; Lonardoni, D.; Nieus, T.; Prato, M.; Scaini, D.; Ballerini, L. From 2D to 3D: Novel Nanostructured Scaffolds to Investigate Signaling in Reconstructed Neuronal Networks. *Sci. Rep.* **2015**, *5*, 9562.
(24) Stetter, O.; Battaglia, D.; Soriano, J.; Geisel, T. Model-Free Reconstruction of Excitatory Neuronal Connectivity from Calcium Imaging Signals. *PLoS Comput. Biol.* **2012**, *8*, e1002653.
(25) Fabbro, A.; Pastore, B.; Nistri, A.; Ballerini, L. Activity-Independent Intracellular Ca^{2+} Oscillations are Spontaneously Generated by Ventral Spinal Neurons during Development *in vitro*. *Cell Calcium* **2007**, *41*, 317−329.
(26) Tibau, E.; Valencia, M.; Soriano, J. Identification of Neuronal Network Properties from the Spectral Analysis of Calcium Imaging Signals in Neuronal Cultures. *Front. Neural Circuits* **2013**, *7*, 199.
(27) Sokal, D. M.; Mason, R.; Parker, T. L. Multi-Neuronal Recordings Reveal a Differential Effect of Thapsigargin on Bicuculline- or Gabazine-Induced Epileptiform Excitability in Rat Hippocampal Neuronal Networks. *Neuropharmacology* **2000**, *39*, 2408−2417.
(28) Raastad, M.; Storm, J. F.; Andersen, P. Putative Single Quantum and Single Fibre Excitatory Postsynaptic Currents Show Similar Amplitude Range and Variability in Rat Hippocampal Slices. *Eur. J. Neurosci.* **1992**, *4*, 113−117.
(29) Bellocchio, E. E.; Reimer, R. J.; Fremeau, R. T., Jr; Edwards, R. H. Uptake of Glutamate into Synaptic Vesicles by an Inorganic Phosphate Transporter. *Science* **2000**, *289*, 957−960.
(30) Moulder, K. L.; Jiang, X.; Taylor, A. A.; Shin, W.; Gillis, K. D.; Mennerick, S. Vesicle Pool Heterogeneity at Hippocampal Glutamate and GABA Synapses. *J. Neurosci.* **2007**, *27*, 9846−9854.
(31) Betz, W. J.; Bewick, G. S. Optical Analysis of Synaptic Vesicle Recycling at the Frog Neuromuscular Junction. *Science* **1992**, *255*, 200−203.
(32) Ryan, T. A.; Reuter, H.; Wendland, B.; Schweizer, F. E.; Tsien, R. W.; Smith, S. J. The Kinetics of Synaptic Vesicle Recycling Measured at Single Presynaptic Boutons. *Neuron* **1993**, *11*, 713−724.
(33) Betz, W.; Mao, F.; Smith, C. Imaging Exocytosis and Endocytosis. *Curr. Opin. Neurobiol.* **1996**, *6*, 365−371.
(34) Ryan, T. A. Presynaptic Imaging Techniques. *Curr. Opin. Neurobiol.* **2001**, *11*, 544−549.
(35) Turola, E.; Furlan, R.; Bianco, F.; Matteoli, M.; Verderio, C. Microglial Microvesicles Secretion and Intercellular Signaling. *Front. Physiol.* **2012**, *3*, 149.
(36) Frühbeis, C.; Fröhlich, D.; Kuo, W. P.; Krämer-Albers, E. M. Extracellular Vesicles as Mediators of Neuron-Glia Communication. *Front. Cell. Neurosci.* **2013**, *7*, 182.
(37) Antonucci, F.; Turola, E.; Riganti, L.; Caleo, M.; Gabrielli, M.; Perrotta, C.; Novellino, L.; Clementi, E.; Giussani, P.; Viani, P.; Matteoli, M.; Verderio, C. Microvesicles Released from Microglia Stimulate Synaptic Activity *via* Enhanced Sphingolipid Metabolism. *EMBO J.* **2012**, *31*, 1231−1240.
(38) Bianco, F.; Pravettoni, E.; Colombo, A.; Schenk, U.; Möller, T.; Matteoli, M.; Verderio, C. Astrocyte-Derived ATP Induces Vesicle Shedding and IL-1 Beta Release from Microglia. *J. Immunol.* **2005**, *174*, 7268−7277.
(39) Bianco, F.; Perrotta, C.; Novellino, L.; Francolini, M.; Riganti, L.; Menna, E.; Saglietti, L.; Schuchman, E. H.; Furlan, R.; Clementi, E.; Matteoli, M.; Verderio, C. Acid Sphingomyelinase Activity Triggers Microparticle Release from Glial Cells. *EMBO J.* **2009**, *28*, 1043−1054.
(40) Del Conde, I.; Shrimpton, C. N.; Thiagarajan, P.; López, J. A. Tissue-Factor-Bearing Microvesicles Arise from Lipid Drafts and Fuse with Activated Platelets to Initiate Coagulation. *Blood* **2005**, *106*, 1604−1611.
(41) Al-Nedawi, K.; Meehan, B.; Micallef, J.; Lhotak, V.; May, L.; Guha, A.; Rak, J. Intercellular Transfer of the Oncogenic Receptor EGFRvIII by Microvesicles Derived from Tumour Cells. *Nat. Cell Biol.* **2008**, *10*, 619−624.
(42) Antonyak, M. A.; Cerione, R. A. Microvesicles as Mediators of Intercellular Communication in Cancer. *Methods Mol. Biol.* **2014**, *1165*, 147−173.
(43) Toyoshima, D.; Mandai, K.; Maruo, T.; Supriyanto, I.; Togashi, H.; Inoue, T.; Mori, M.; Takai, Y. Afadin Regulates Puncta Adherentia Junction Formation and Presynaptic Differentiation in Hippocampal Neurons. *PLoS One* **2014**, *9*, e89763.
(44) Aguado, F.; Carmona, M. A.; Pozas, E.; Aguiló, A.; Martínez-Guijarro, F. J.; Alcantara, S.; Borrell, V.; Yuste, R.; Ibañez, C. F.; Soriano, E. BDNF Regulates Spontaneous Correlated Activity at Early Developmental Stages by Increasing Synaptogenesis and Expression of the K^+/Cl^- Co-Transporter KCC2. *Development* **2003**, *130*, 1267−1280.
(45) Chong, Y.; Ge, C.; Yang, Z.; Garate, J. A.; Gu, Z.; Weber, J. K.; Liu, J.; Zhou, R. Reduced Cytotoxicity of Graphene Nanosheets Mediated by Blood-Protein Coating. *ACS Nano* **2015**, *9*, 5713−5724.
(46) Fabbro, A.; Sucapane, A.; Toma, F. M.; Calura, E.; Rizzetto, L.; Carrieri, C.; Roncaglia, P.; Martinelli, V.; Scaini, D.; Masten, L.; Turco, A.; Gustincich, S.; Prato, M.; Ballerini, L. Adhesion to Carbon Nanotube Conductive Scaffolds Forces Action-Potential Appearance in Immature Rat Spinal Neurons. *PLoS One* **2013**, *8*, e73621.
(47) Malarkey, E. B.; Reyes, R. C.; Zhao, B.; Haddon, R. C.; Parpura, V. Water Soluble Single-Walled Carbon Nanotubes Inhibit Stimulated Endocytosis in Neurons. *Nano Lett.* **2008**, *8*, 3538−3542.
(48) High, B.; Cole, A. A.; Chen, X.; Reese, T. S. Electron Microscopic Tomography Reveals Discrete Transcleft Elements at Excitatory and Inhibitory Synapses. *Front. Synaptic Neurosci.* **2015**, *7*, 9.
(49) Fedorovich, S. V.; Alekseenko, A. V.; Waseem, T. V. Are Synapses Targets of Nanoparticles? *Biochem. Soc. Trans.* **2010**, *38*, 536−538.
(50) Grados, M. A.; Atkins, E. B.; Kovacikova, G. I.; McVicar, E. A Selective Review of Glutamate Pharmacological Therapy in Obsessive-Compulsive and Related Disorders. *Psychology Res. and Behavior Management PRBM* **2015**, *8*, 115−131.
(51) Gardoni, F.; Di Luca, M. Targeting Glutamatergic Synapses in Parkinson's Disease. *Curr. Opin. Pharmacol.* **2015**, *20*, 24−28.
(52) Stone, J. M. Glutamatergic Antipsychotic Drugs: a New Dawn in the Treatment of Schizophrenia? *Ther. Adv. Psychopharmacol.* **2011**, *1*, 5−18.
(53) Meyer, R. A.; Sunshine, J. C.; Green, J. J. Biomimetic Particles as Therapeutics. *Trends Biotechnol.* **2015**, *33*, 514−524.
(54) Borisova, T.; Nazarova, A.; Dekaliuk, M.; Krisanova, N.; Pozdnyakova, N.; Borysov, A.; Sivko, R.; Demchenko, A. P. Neuromodulatory Properties of Fluorescent Carbon Dots: Effect on Exocytotic Release, Uptake and Ambient Level of Glutamate and GABA in Brain Nerve Terminals. *Int. J. Biochem. Cell Biol.* **2015**, *59*, 203−215.
(55) Fabbro, A.; Scaini, D.; León, V.; Vázquez, E.; Cellot, G.; Privitera, G.; Lombardi, L.; Torrisi, F.; Tomarchio, F.; Bonaccorso, F.; Bosi, S.; Ferrari, A. C.; Ballerini, L.; Prato, M. Graphene-Based Interfaces Do Not Alter Target Nerve Cells. *ACS Nano* **2016**, *10*, 615−23.
(56) Ali-Boucetta, H.; Bitounis, D.; Raveendran-Nair, R.; Servant, A.; Van den Bossche, J.; Kostarelos, K. Purified Graphene Oxide Dispersions Lack *in vitro* Cytotoxicity and *in vivo* Pathogenicity. *Adv. Healthcare Mater.* **2013**, *2*, 433−441.
(57) Mukherjee, S. P.; Lozano, N.; Kucki, M.; Del-Rio Castillo, A. E.; Vázquez, E.; Kostarelos, K.; Wick, P.; Fadeel, B. Detection of Endotoxin Contamination of Graphene Oxide Using the TNF-α Expression Test and Guidelines for Endotoxin-Free Graphene Oxide Production. Submitted for publication.
(58) Jasim, D. A.; Lozano, N.; Kostarelos, K. Synthesis of Few-Layered, High-Purity Graphene Oxide Sheets from Different Graphite Sources for Biology. *2D Mater.* **2016**, *3*, 014006.

DOI: 10.1021/acsnano.6b00130
ACS Nano 2016, 10, 4459−4471

(59) Varela-Rizo, H.; Rodriguez-Pastor, I.; Merino, C.; Martin-Gullon, I. Highly Crystalline Graphene Oxide Nano-Platelets Produced From Helical-Ribbon Carbon Nanofibers. *Carbon* **2010**, *48*, 3640−3643.
(60) Cellot, G.; Cilia, E.; Cipollone, S.; Rancic, V.; Sucapane, A.; Giordani, S.; Gambazzi, L.; Markram, H.; Grandolfo, M.; Scaini, D.; Gelain, F.; Casalis, L.; Prato, M.; Giugliano, M.; Ballerini, L. Carbon Nanotubes Might Improve Neuronal Performance by Favouring Electrical Shortcuts. *Nat. Nanotechnol.* **2009**, *4*, 126−133.
(61) Calegari, F.; Coco, S.; Taverna, E.; Bassetti, M.; Verderio, C.; Corradi, N.; Matteoli, M.; Rosa, P. A Regulated Secretory Pathway in Cultured Hippocampal Astrocytes. *J. Biol. Chem.* **1999**, *274*, 22539−22547.
(62) Pavlidis, P.; Montgomery, J.; Madison, D. V. Presynaptic Protein Kinase Activity Supports Long-Term Potentiation at Synapses Between Individual Hippocampal Neurons. *J. Neurosci.* **2000**, *20*, 4497−4505.
(63) Hoopmann, P.; Rizzoli, S. O.; Betz, W. J. Imaging Synaptic Vesicle Recycling by Staining and Destaining Vesicles with FM Dyes. *Cold Spring Harbor Protoc.* **2012**, *1*, 77−83.
(64) Schindelin, J.; Arganda-Carreras, I.; Frise, E.; Kaynig, V.; Longair, M.; Pietzsch, T.; Preibisch, S.; Rueden, C.; Saalfeld, S.; Schmid, B.; Tinevez, J. Y.; White, D. J.; Hartenstein, V.; Eliceiri, K.; Tomancak, P.; Cardona, A. Fiji: An Open-Source Platform for Biological-Image Analysis. *Nat. Methods* **2012**, *9*, 676−682.
(65) Junker, J. P.; Rief, M. Single-Molecule Force Spectroscopy Distinguishes Target Binding Modes of Calmodulin. *Proc. Natl. Acad. Sci. U. S. A.* **2009**, *106*, 14361−14366.
(66) Klapetek, P.; Valtr, M.; Nečas, D.; Salyk, O.; Dzik, P. Atomic Force Microscopy Analysis of Nanoparticles in Non-Ideal Conditions. *Nanoscale Res. Lett.* **2011**, *6*, 514.

DOI: 10.1021/acsnano.6b00130
ACS Nano 2016, 10, 4459−4471